



# Technical note: A comparative study of chemistry schemes for volcanic sulfur dioxide in Lagrangian transport simulations – a case study of the 2019 Raikoke eruption

Mingzhao Liu<sup>1,2</sup>, Lars Hoffmann<sup>1,2</sup>, Jens-Uwe Grooß<sup>3,2</sup>, Zhongyin Cai<sup>4</sup>, Sabine Grießbach<sup>1,2</sup>, and Yi Heng<sup>5</sup>

<sup>1</sup>Jülich Supercomputing Centre, Forschungszentrum Jülich, Jülich, Germany

<sup>2</sup>Center for Advanced Simulation and Analytics (CASA), Forschungszentrum Jülich, Jülich, Germany

<sup>3</sup>Institute of Climate and Energy Systems, Stratosphere (ICE-4), Forschungszentrum Jülich, Jülich, Germany

<sup>4</sup>Yunnan Key Laboratory of International Rivers and Transboundary Eco-security, Institute of International Rivers and Eco-Security, Yunnan University, Kunming, China

<sup>5</sup>School of Computer Science and Engineering, Sun Yat-sen University, Guangzhou, China

**Correspondence:** Mingzhao Liu (mi.liu@fz-juelich.de)

Received: 16 August 2024 – Discussion started: 9 September 2024

Revised: 10 January 2025 – Accepted: 30 January 2025 – Published: 23 April 2025

**Abstract.** Lagrangian transport models are important tools to study the sources, spread, and lifetime of air pollutants. In order to simulate the transport of reactive atmospheric pollutants, the implementation of efficient chemistry and mixing schemes is necessary to properly represent the lifetime of chemical species. Based on a case study simulating the long-range transport of volcanic sulfur dioxide (SO<sub>2</sub>) for the 2019 Raikoke eruption, this study compares two chemistry schemes implemented in the Massive-Parallel Trajectory Calculations (MPTRAC) Lagrangian transport model. The explicit scheme represents first-order and pseudo-first-order loss processes of SO<sub>2</sub> based on prescribed reaction rates and climatological oxidant fields, i.e., the hydroxyl radical in the gas phase and hydrogen peroxide in the aqueous phase. Furthermore, an implicit scheme with a reduced chemistry mechanism for volcanic SO<sub>2</sub> decomposition has been implemented, targeting the upper-troposphere–lower-stratosphere (UT–LS) region. Considering nonlinear effects of the volcanic SO<sub>2</sub> chemistry in the UT–LS region, we found that the implicit solution yields a better representation of the volcanic SO<sub>2</sub> lifetime, while the first-order explicit solution has better computational efficiency. By analyzing the dependence between the oxidants and SO<sub>2</sub> concentrations, correction formulas are derived to adjust the oxidant fields used in the explicit solution, leading to a good trade-off between computational efficiency and accuracy. We consider this work to be an important step forward to support future research on emission source reconstruction involving nonlinear chemical processes.

## 1 Introduction

Lagrangian transport models simulate the trajectories of air parcels that carry trace gases and aerosols through the atmosphere. These trajectories are determined using external datasets, which provide horizontal wind and vertical velocity fields obtained from meteorological reanalyses or forecast

models. Lagrangian transport models are particularly useful for studying complex atmospheric processes, such as the interaction between different pollutants, chemical transformations, and the influence of different meteorological conditions. Lagrangian transport models have been widely applied in studies of natural and anthropogenic pollutant emissions. Applications of Lagrangian models include the simulation of

point source or regional pollutant emissions, such as volcanic eruptions (Webster and Thomson, 2022), nuclear leakage accidents (Stohl et al., 2012), or wildfires (Evangelidou et al., 2019). They can also be used for global chemical transport simulations and source estimations of greenhouse gases such as carbon dioxide (CO<sub>2</sub>) or methane (CH<sub>4</sub>) (Bergamaschi et al., 2022; Che et al., 2022), long-lived gases of chlorofluorocarbons (CFCs) or hydrofluorocarbons (HFCs) (Pommrich et al., 2014; Brunner et al., 2017), fossil emissions (Dalsøren et al., 2018), and more. In contrast to grid-based Eulerian models, which represent fluid transport at fixed grid locations and suffer from numerical diffusion due to limited grid resolution, trajectory-based Lagrangian models generally have much lower numerical diffusion. In addition, Lagrangian models have the specific advantage of high scalability and computational efficiency, making them suitable for long-range and large-scale simulations. When simulating a large number of chemical species, Lagrangian models do not need to calculate transport separately for each species as in a grid-based Eulerian scheme (Brunner, 2012). However, Lagrangian models can face challenges such as complex boundary condition handling, difficulties in representing concentration fields and physical diffusion, high particle requirements for dense regions, and uneven computational loads.

In the past, Lagrangian models have often been used to qualitatively identify the source and reproduce the spatial distribution of plumes of trace gases, e.g., by tracking air parcels backward in time from receptors to sources to reconstruct the emissions (Wu et al., 2017; Pardini et al., 2017). In case studies of volcanic eruptions, the effects of SO<sub>2</sub> lifetime variations with altitude are usually neglected. However, Lagrangian models have the potential to be more quantitative. The essential step is to accurately model the physical and chemical processes for accurate prediction of the species' lifetime. For atmospheric species, such as SO<sub>x</sub>, NO<sub>x</sub>, hydrocarbons, and halocarbons, the chemical reactions have a significant impact on the estimation of their sources and sinks. Uncertainties introduced by chemical sinks can strongly influence the top-down source estimation (Stavrakou et al., 2013).

In the Lagrangian framework, the motion of species is simplified to time integration along trajectories determined by meteorological data. Species sinks are modeled separately for each air parcel, specifying the time derivative of the mass or mixing ratio of each species with an explicit rate. This method can represent processes such as dry/wet deposition, sedimentation, and first-order chemical reactions. For example, Liu et al. (2023) simulated the evolution of the SO<sub>2</sub> mass burden from the 2018 Ambae eruption with explicit loss rates, including wet deposition and gas-phase and aqueous-phase reactions, and they discussed the height sensitivity of SO<sub>2</sub> loss rates related to cloud distributions. For bimolecular or second-order reactions, where rates depend on the concentrations of two species, Liu et al. (2023) prescribed monthly zonal mean climatologies for OH and H<sub>2</sub>O<sub>2</sub> to ob-

tain pseudo-first-order approximations of the SO<sub>2</sub> oxidation. However, in dense volcanic SO<sub>2</sub> plumes, this approach may fail to capture oxidant depletion due to reactions with SO<sub>2</sub>, particularly in regions of high SO<sub>2</sub> concentration. Accurate simulations under these conditions require dynamic coupling between reactant concentrations and reaction rates to properly represent second-order processes.

To model nonlinear chemical processes, an implicit chemical solver and an atmospheric mixing scheme should be considered (Brunner, 2012). In essence, while Lagrangian models efficiently track particle trajectories, a mixing scheme is essential to accurately represent diffusion and produce smooth gradients in concentration fields. Without a mixing scheme, particles carrying different reactants may remain isolated, resulting in pronounced local irregularities and inaccurate reaction rates. Mixing schemes address these issues by smoothing out irregularities in particle distributions, improving physical realism, and ensuring numerical stability. In recent years, three main types of Lagrangian chemical and mixing schemes have been considered. The first scheme uses a dynamically adaptive grid algorithm to mimic the stretching and distortion of air, such as in the Chemical Lagrangian Model of the Stratosphere (CLaMS) (McKenna et al., 2002b, a) and the Alfred Wegener Institute Lagrangian Chemistry/Transport System (ATLAS) (Wohltmann and Rex, 2009). The second scheme implements the chemistry scheme on a fixed 3-D grid, assuming uniform mixing of individual species within the grid boxes, such as in the UK Met Office's Next-Generation Atmospheric Dispersion Model (NAME) (Redington et al., 2009) and the Hybrid Single-Particle Lagrangian Integrated Trajectory (HYSPLIT) (Stein et al., 2000) model. The third scheme implements the chemistry scheme on the Lagrangian air parcels, but it uses a parameter to control the degree of mixing by adding a term to relax the trace gas concentrations in the air parcels to the background values averaged over a fixed 3-D grid, which is applied by the UK Meteorological Office (UKMO) chemistry transport model (STOCHEM) (Stevenson et al., 1998).

This paper focuses on the chemistry scheme implementation in the Massive Parallel Trajectory Calculations (MPTRAC) Lagrangian transport model (Hoffmann et al., 2016, 2022). Here, we selected the third approach outlined above, as it allows for online coupling of chemistry calculations with trajectory calculations, performed separately for each air parcel, followed by inter-parcel mixing, making it particularly suitable for large-scale parallelization. MPTRAC is designed for large-scale atmospheric simulations on high-performance computing (HPC) systems and has a hybrid message passing interface (MPI)–open multiprocessing (OpenMP)–open accelerator (OpenACC) parallelization scheme implemented, demonstrating excellent performance and scalability on both CPUs (Liu et al., 2020) and GPUs (Hoffmann et al., 2024b). The model has been used in several case studies to simulate the long-range trans-

port of volcanic SO<sub>2</sub>, with emission estimates obtained from a backward-trajectory method (Wu et al., 2017, 2018; Cai et al., 2022) and a more complex and computationally intensive inverse modeling approach (Heng et al., 2016). In those studies, the height-dependent lifetime of SO<sub>2</sub> was not considered to be an influencing factor, as older versions of MPTRAC did not have a detailed chemistry scheme.

The main objective of this study is to introduce and assess a newly developed chemistry scheme with an implicit chemistry solver in the MPTRAC model that improves long-range chemistry transport simulations of volcanic SO<sub>2</sub> and allows for the estimation of volcanic emission sources. We propose a small chemical mechanism with 12 species and 31 reactions to model the production and loss of OH, HO<sub>2</sub>, and H<sub>2</sub>O<sub>2</sub> in the upper-troposphere–lower-stratosphere (UT–LS) region, including reactions among O(<sup>1</sup>D), O(<sup>3</sup>P), H, OH, HO<sub>2</sub>, O<sub>3</sub>, and H<sub>2</sub>O; reactions of SO<sub>2</sub> with OH in the gas phase; and oxidation with H<sub>2</sub>O<sub>2</sub> in the aqueous phase. The aim is to model the dynamic OH and H<sub>2</sub>O<sub>2</sub> fields as SO<sub>2</sub> oxidants to more realistically simulate and better represent the chemical lifetime of volcanic SO<sub>2</sub> in the UT–LS region. The chemical solver was built using the Kinetic Preprocessor (KPP) software package (Damian et al., 2002; Sandu and Sander, 2006). The KPP software provides a framework to automatically generate a Rosenbrock integrator for solving the stiff ordinary differential equations with specification of a chemical mechanism, including the chemical equations, species, and rate coefficients. The KPP has been widely used in atmospheric chemical modeling, for instance, in GEOS-Chem (Henze et al., 2007) and MECCA (Sander et al., 2019).

In a case study, we conducted simulations of the June 2019 Raikoke volcanic eruption to compare and verify the modeled lifetime of the SO<sub>2</sub> emissions with TROPospheric Monitoring Instrument (TROPOMI) satellite measurements (Veefkind et al., 2012; Theys et al., 2017). The Raikoke (48.17° N, 152.15° E) eruption was a notable event that has been discussed in the literature to some larger extent. The eruption on 21–22 June was characterized by a series of explosive events that emitted SO<sub>2</sub> and volcanic ash into the lower stratosphere, impacting the stratospheric aerosol layer (Gorkavyi et al., 2021; Kloss et al., 2021). Cai et al. (2022) used MPTRAC to estimate the SO<sub>2</sub> emissions and investigate the effects of the injection height, time, and diffusion parameters on the simulation results. With an estimated  $1.5 \pm 0.2$  Tg of SO<sub>2</sub>, the eruption was notable for being the largest SO<sub>2</sub> injection into the upper troposphere and lower stratosphere since the 2011 Nabro eruption (Cai et al., 2022). In their publication, de Leeuw et al. (2021) discuss the transport and chemical evolution of SO<sub>2</sub> emissions resulting from the 2019 Raikoke eruption, offering a comprehensive comparison between NAME model simulations and TROPOMI observations.

This paper is organized as follows: in Sect. 2, we introduce the MPTRAC model, including the details of the implementation of the chemistry schemes, and the TROPOMI SO<sub>2</sub>

satellite dataset; in Sect. 3, we discuss the results of the Lagrangian chemical transport simulations with MPTRAC for the Raikoke eruption, including the evaluation of the modeled SO<sub>2</sub> fields in the UT–LS region with the satellite data; and, finally, Sect. 4 provides the summary and conclusions of the study.

## 2 Data and methods

### 2.1 Overview on the MPTRAC model

Massive-Parallel Trajectory Calculations (MPTRAC) is a Lagrangian transport model that has been designed for heterogeneous CPU/GPU HPC systems and is particularly suitable for large-scale and long-term atmospheric simulations in the free troposphere and stratosphere (Hoffmann et al., 2016, 2022). The model requires meteorological input fields, in particular the horizontal wind and vertical velocity fields for the kinematic trajectory calculations, the temperature field for the chemistry calculations, and the cloud water fields for wet deposition and aqueous-phase chemistry. The trajectories of the air parcels are calculated using the explicit mid-point method to maintain the balance between computational efficiency and accuracy (Röbler et al., 2018). Following Stohl et al. (2005), diffusion is represented via stochastic perturbations added to the position of the air parcels, and subgrid-scale wind fluctuations are modeled as a Markov process using the Langevin equation. Unresolved convection is modeled via the extreme convection parametrization (Gerbig et al., 2003; Hoffmann et al., 2023). A comprehensive description of the model is given by Hoffmann et al. (2022). In the following section, we will discuss the two chemistry schemes implemented in the model in more detail.

Lagrangian transport simulations with MPTRAC are driven by global meteorological reanalyses or forecasts. Here, we applied the fifth-generation reanalysis (ERA5; Hersbach et al., 2020) from the European Centre for Medium-Range Weather Forecasts (ECMWF); this reanalysis provides hourly meteorological data at a  $0.3^\circ \times 0.3^\circ$  horizontal resolution on 137 vertical levels from the surface up to 0.01 hPa. Utilizing a state-of-the-art data assimilation system, ERA5 integrates a vast array of historical observations, including satellite and in situ data, to generate consistent, accurate, and temporally continuous records of meteorological information from the year 1950 to the present. The ERA5 data provide significant improvements with respect to meteorological information compared with the previous-generation ERA-Interim reanalysis (Dee et al., 2011), thereby benefiting the accuracy of Lagrangian transport simulations (Hoffmann et al., 2019).

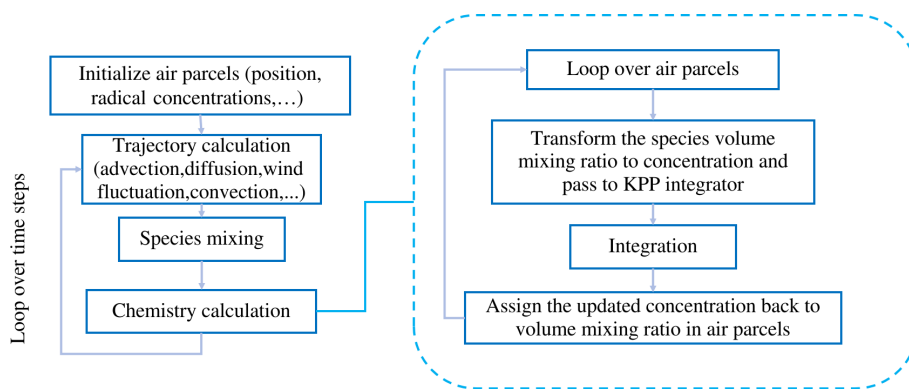


**Figure 1.** Simplified flow chart of the Massive-Parallel Trajectory Calculations (MPTRAC) Lagrangian chemistry transport model.

## 2.2 Chemistry schemes and mixing in MPTRAC

### 2.2.1 First-order explicit chemistry scheme

In a Lagrangian model, linear decay processes over time  $t$  can be expressed as follows:

$$\frac{dy}{dt} = ky, \quad (1)$$

where  $y$  represents the mass or volume mixing ratio (VMR) of a species in an air parcel. For a constant loss rate  $k$ , this ordinary differential equation is solved explicitly using the following exponential equation:

$$y(t + \Delta t) = y(t)e^{-k\Delta t}. \quad (2)$$

Here, the rate coefficient  $k$  is prescribed as a model input. In MPTRAC, various loss processes such as wet/dry deposition or sedimentation are modeled in this way. When solving first-order chemical reactions, e.g., photolysis, the explicit solution has good computational efficiency, as it does not require numerical integration. The reactions of long-lived tracers with short-lived radicals can also be treated as pseudo-first-order reactions, assuming that production and loss of the radicals are in equilibrium and the pseudo-first-order rate constant  $k$  can be expressed as the product of the second-order rate coefficient  $k_{2\text{nd}}$  and the concentration of the oxidant  $[X]$ , i.e.,  $k = k_{2\text{nd}}[X]$ .

In MPTRAC, prescribed radical species concentrations are taken from a monthly zonal mean climatology of Pommrich et al. (2014), which was prepared with the CLaMS model. In contrast to MPTRAC, which focuses on efficient particle transport with limited or simplified chemistry, the CLaMS model emphasizes detailed chemical reaction schemes for stratospheric processes. We consider the CLaMS model a reliable source for creating radical species climatologies for the UT–LS region. Following Liu et al. (2023), the OH field is scaled with a correction factor based on the solar zenith angle to mimic diurnal variations while preserving daily averages. Similarly, the monthly zonal mean H<sub>2</sub>O<sub>2</sub> background field

was obtained from the Copernicus Atmosphere Monitoring Service (CAMS) reanalysis (Inness et al., 2019) compiled into a monthly zonal mean climatology. At each time step, background field values are interpolated from the tabulated zonal mean data according to the pressure and latitude of the air parcels.

Regarding the SO<sub>2</sub> chemical reactions, the gas-phase oxidation with OH and the aqueous-phase oxidation with H<sub>2</sub>O<sub>2</sub> are considered. In the cloud aqueous phase, H<sub>2</sub>O<sub>2</sub> oxidation is the predominant pathway when pH < 5 (Seinfeld and Pandis, 2016; Rolph et al., 1992; Pattantyus et al., 2018). Other aqueous-phase oxidation pathways such as ozone oxidation and catalyzed oxidation via Fe(III) and Mn(II) are neglected because of low pH values in highly concentrated SO<sub>2</sub> volcanic plumes. Liu et al. (2023) conducted a case study of the 2018 Ambae eruption with the first-order simplified chemistry scheme of MPTRAC, which provides more details.

### 2.2.2 Implicit chemistry scheme

Figure 1 shows a simplified flow chart of the MPTRAC model, including details of the chemistry calculations. The chemistry calculations follow the trajectory calculations and the mixing process. At each chemistry time step, the species' VMRs of each air parcel are multiplied by the molecular density of air to convert them into concentration units (molecules cm<sup>-3</sup>). After numerical integration of the chemical mechanism with the KPP integrator, the updated concentrations evolved in time are converted back to VMRs and assigned back to each air parcel. The chemical processes of different air parcels are calculated independently of each other, making this an ideal parallel-computing problem, which is particularly suitable for parallelization.

Our proposed chemistry mechanism for the decomposition of volcanic SO<sub>2</sub> in the UT–LS region includes 31 reactions and 12 species, as detailed in Table 1. This specific mechanism is newly proposed and has not been published or evaluated elsewhere. We developed the mechanism

**Table 1.** Proposed chemistry scheme for volcanic SO<sub>2</sub> oxidation in the UT–LS region.

Index	Reaction
R1	$O(^3P) + O_2 \rightarrow O_3$
R2	$O(^3P) + O_3 \rightarrow 2O_2$
R3	$O(^3P) + OH \rightarrow O_2 + H$
R4	$O(^3P) + HO_2 \rightarrow OH + O_2$
R5	$O(^3P) + H_2O_2 \rightarrow OH + HO_2$
R6	$O(^1D) + O_2 \rightarrow O(^3P) + O_2$
R7	$O(^1D) + O_3 \rightarrow 2O(^3P) + O_2$
R8	$O(^1D) + H_2 \rightarrow OH + H$
R9	$O(^1D) + H_2O \rightarrow 2OH$
R10	$O(^1D) + N_2 \rightarrow O(^3P) + N_2$
R11	$O(^1D) + N_2 \rightarrow N_2O$
R12	$O(^1D) + N_2O \rightarrow \text{products}$
R13	$H + O_2 \rightarrow HO_2$
R14	$H + O_3 \rightarrow OH + O_2$
R15	$H + HO_2 \rightarrow 2OH$
R16	$H + HO_2 \rightarrow O(^3P) + H_2O$
R17	$H + HO_2 \rightarrow H_2 + O_2$
R18	$OH + O_3 \rightarrow HO_2 + O_2$
R19	$OH + OH \rightarrow H_2O + O(^3P)$
R20	$OH + OH \rightarrow H_2O_2$
R21	$OH + HO_2 \rightarrow H_2O + O_2$
R22	$OH + H_2O_2 \rightarrow H_2O + HO_2$
R23	$HO_2 + O_3 \rightarrow OH + 2O_2$
R24	$HO_2 + HO_2 \rightarrow O_2 + H_2O_2$
R25	$O_2 + h\nu \rightarrow 2O(^3P)$
R26	$O_3 + h\nu \rightarrow O(^1D) + O_2$
R27	$O_3 + h\nu \rightarrow O(^3P) + O_2$
R28	$H_2O + h\nu \rightarrow H + OH$
R29	$H_2O_2 + h\nu \rightarrow 2OH$
R30	$SO_2 + H_2O_2(\text{aq}) \rightarrow \text{products}$
R31	$SO_2 + OH \rightarrow \text{products}$

starting from SO<sub>2</sub> oxidation via OH in the gas phase (Reaction R31) and oxidation via H<sub>2</sub>O<sub>2</sub> in the aqueous phase (Reaction R30), which are the major loss mechanisms for volcanic SO<sub>2</sub> (Rolph et al., 1992; Pattantyus et al., 2018; de Leeuw et al., 2021). Next, we integrated further reactions to model the dynamic production and loss of OH and H<sub>2</sub>O<sub>2</sub>.

The production of OH mainly occurs via the reaction of H<sub>2</sub>O with the excited oxygen radical O(<sup>1</sup>D) (Reaction R9). The OH concentration exhibits a clear diurnal variation, due to a strong relationship with solar radiation (Reactions R25–R29), and a short lifetime resulting from self-reaction (Reactions R19 and R20) and reactions with O<sub>3</sub> (Reaction R18) and H<sub>2</sub>O (Reaction R21) (Minschwaner et al., 2011; Tan et al., 2019). The H<sub>2</sub>O<sub>2</sub> is primarily formed through the self-reaction of hydroperoxy radicals (HO<sub>2</sub>) (Reaction R24), which are mainly produced via H and O<sub>2</sub> (Reaction R13) (Rieger et al., 2018). We incorporated additional reactions into the chemical mechanism, even though they are less rel-

evant to the primary focus of volcanic SO<sub>2</sub> decomposition in the UT–LS, to capture potential secondary effects that might influence the system under certain conditions or improve applicability.

Note that this scheme for the oxidation of SO<sub>2</sub> was not designed for application in the boundary layer and lower troposphere, as it excludes nitrogen oxides, hydrocarbons, and carbon monoxide emissions and reactions. Furthermore, to simplify and constrain the chemistry calculations, each air parcel's ozone VMR is updated at every chemistry time step using ERA5 reanalysis data interpolation. Water vapor is also updated using ERA5 reanalysis data. The rate coefficients of all chemical reactions were taken from the current recommendations of Burkholder et al. (2019).

For photolysis modeling, we created 3-D photolysis rate look-up tables for the different species,  $J = J(\theta_s, \text{TCO}, p)$ , where  $\theta_s$  is the solar zenith angle, TCO is total column ozone, and  $p$  is pressure. The photolysis rate look-up tables cover 33 solar zenith angles from 0 to 96°, 8 total column ozone levels from 100 to 450 DU, and 66 pressure levels from 1013.25 to 0.1 hPa. The look-up tables were generated using the DISSOC photolysis module of CLaMS, originally based on Lary and Pyle (1991) and improved over time in several studies (Becker et al., 2000; Hoppe et al., 2014; Pommrich et al., 2014). Note that, for the DISSOC photochemistry model, we established the relationship between pressure, temperature, and ozone density via the U.S. Committee on Extension to the Standard Atmosphere (1976). The MPTRAC chemistry code determines  $\theta_s$ , TCO, and  $p$  for each air parcel and linearly interpolates the corresponding  $J$  values from the look-up tables. The look-up table approach has the advantages of high computational efficiency and easy implementation on both GPUs and CPUs.

### 2.3 Wet deposition

Although the primary focus of this study is the comparison between the explicit and implicit chemistry schemes, it is also important to briefly outline the treatment of wet deposition in the MPTRAC model, as this is another significant loss process for volcanic SO<sub>2</sub> in cloud-containing environments. Wet deposition refers to the removal of SO<sub>2</sub> through processes such as precipitation scavenging, where SO<sub>2</sub> is dissolved in water droplets or ice crystals and subsequently removed from the atmosphere. Although the focus of this study is on chemical losses, it is crucial to consider wet deposition, particularly in tropical regions or during eruptions with high levels of atmospheric moisture, as it can significantly influence the lifetime of SO<sub>2</sub> and its transport in volcanic plumes. The interplay between wet deposition and chemical reactions in the presence of clouds contributes to the overall removal of SO<sub>2</sub> from the atmosphere, which is essential for accurate modeling of volcanic emissions and their impact on atmospheric chemistry.

In MPTRAC, wet deposition is implemented as a first-order loss term, where the removal rate of SO<sub>2</sub> depends on its concentration in the air parcel and the cloud water content. The in-cloud wet deposition rate is modeled via a rain-out process that considers the solubility of SO<sub>2</sub> and the precipitation rate, while the below-cloud deposition is represented by an empirical exponential formula based on precipitation intensity. This framework enables the model to account for the effects of cloud coverage and precipitation on SO<sub>2</sub> removal in both the gas and aqueous phase. The methodology for wet deposition in MPTRAC is detailed in Hoffmann et al. (2022) and has been modified and extended to address volcanic SO<sub>2</sub> deposition in Liu et al. (2023). Wet deposition has been considered in all simulations discussed in this paper.

## 2.4 Inter-parcel mixing algorithm

As mentioned in Sect. 1, atmospheric mixing is particularly important for properly modeling chemistry and transport in Lagrangian models (Brunner, 2012). The Lagrangian method inherently avoids numerical diffusion. A parameterization of mixing needs to be included to simulate transport and chemistry in a realistic manner. Here, we adapted the inter-parcel mixing scheme of Collins et al. (1997). This mixing scheme has the advantages of simple implementation and being well suited to CPU and GPU parallelization.

Following Collins et al. (1997), a relaxation term  $d(c - \bar{c})$  is added to bring the VMR value  $c$  of each air parcel closer to the average value  $\bar{c}$  within fixed grid boxes. A mixing parameter of  $d = 0$  means there is no mixing whereas a mixing parameter of  $d = 1$  means the species VMR is fully relaxed to the grid box mean. The parameter  $d$  therefore controls the degree of mixing. Default values of  $d$  are taken from Stevenson et al. (1998) to be  $10^{-3}$  in the troposphere and  $10^{-6}$  in the stratosphere. The grid box size was set to  $5^\circ \times 5^\circ \times 1$  km (longitude  $\times$  latitude  $\times$  log-pressure height). Mixing was conducted at every time step of the model, which is 180 s in this case.

## 2.5 TROPOMI SO<sub>2</sub> observations

In order to validate the simulated volcanic SO<sub>2</sub> distributions and lifetime for the Raikoke eruption, we used the Tropospheric Monitoring Instrument (TROPOMI) SO<sub>2</sub> Level 2 data product (Veeffkind et al., 2012; Theys et al., 2017). TROPOMI is an ultraviolet, visible, near-infrared, and short-wavelength infrared spectrometer. It is mounted on the European Space Agency's Sentinel-5P satellite. The satellite operates in a near-polar Sun-synchronous orbit with an equatorial crossing time of 13:30 LT (local time) for the ascending nodes. TROPOMI samples the Earth's surface and atmosphere with a spatial resolution of  $7 \times 3.5$  km<sup>2</sup> over a swath width of 2600 km. TROPOMI monitors ozone, methane, formaldehyde, aerosol, carbon monoxide, NO<sub>2</sub>, and SO<sub>2</sub> in the atmosphere.

The TROPOMI Level 2 data include three SO<sub>2</sub> data products that provide SO<sub>2</sub> total column densities derived assuming a 1 km deep SO<sub>2</sub> layer centered at altitudes of 1, 7, and 15 km. In this study, we used the 15 km product because it best fits the SO<sub>2</sub> mass release from Raikoke volcano into the UT–LS region. To obtain the SO<sub>2</sub> total mass burden, we first averaged the TROPOMI retrieval data over horizontal grid boxes of  $0.1^\circ \times 0.1^\circ$  and then integrated the averaged values of the grid boxes. Note that the TROPOMI SO<sub>2</sub> total column data are provided in Dobson units (hereafter denoted using DU). This is similar to ozone measurements; however, for SO<sub>2</sub>, 1 DU corresponds to a total column density of  $2.85 \times 10^{-5}$  kg m<sup>-2</sup>. A lower bound of 0.35 DU was applied to both the satellite measurements and the model results to reduce the effect of noise from the satellite measurements and to improve comparisons.

## 3 Results of the Raikoke case study

### 3.1 Model initialization and baseline simulation

In an earlier study, Cai et al. (2022) investigated the time- and height-resolved SO<sub>2</sub> injection parameters of the 2019 Raikoke eruption based on a backward-trajectory approach and SO<sub>2</sub> retrievals from TROPOMI observations. In this work, we used the same estimates of the SO<sub>2</sub> injections (as Cai et al., 2022) to initialize the release of air parcels in the transport simulations. A total SO<sub>2</sub> mass of 1.6 Tg was distributed over  $10^6$  air parcels. The main injection peak occurs between 21 and 22 June 2019 at altitudes between 5 and 15 km. The vertical profile of the SO<sub>2</sub> injection rates is shown in Fig. 2. Numerical experiments were conducted with MPTRAC to compare the results of the linear-explicit and nonlinear-implicit chemistry solutions. Here, the simplified explicit approximation scheme is similar to the work of Liu et al. (2023), considering the gas-phase oxidation and aqueous-phase oxidation with climatological background OH and H<sub>2</sub>O<sub>2</sub> fields (as introduced in Sect. 2.2.1). The KPP implicit solution considers the same reactions of SO<sub>2</sub>, but the OH and H<sub>2</sub>O<sub>2</sub> fields are modeled with the chemical mechanism listed in Table 1.

The simulated SO<sub>2</sub> plume evolution with the KPP implicit chemistry scheme is compared with TROPOMI observations in Figs. 3 and 4. The explicit scheme closely matches the implicit scheme with respect to plume shape (not shown) but shows overall lower SO<sub>2</sub> column densities due to higher OH oxidation loss rates. Based on these comparisons, the MPTRAC model effectively captures the dispersion and transport of the volcanic SO<sub>2</sub> plume during the first 10 d after the eruption. Both the TROPOMI retrievals and the MPTRAC simulations show that the SO<sub>2</sub> plume continuously spreads over a larger area, with significant eastward motion and following the cyclonic flows. Consistent with the findings of Cai et al. (2022) and de Leeuw et al. (2021), the accuracy of the model results in reproducing the struc-

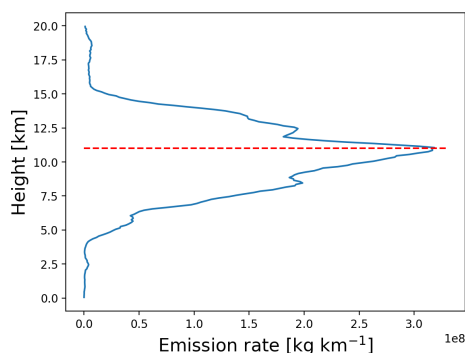


**Figure 2.** Vertical profile of SO<sub>2</sub> injections from the Raikoke eruption, as estimated by Cai et al. (2022). The red line represents the tropopause height at the location of the volcano.

tural features of the observed SO<sub>2</sub> distributions gradually decrease after 15 d of simulation time due to error propagation. This decline is attributed to the limited resolution of the meteorological data, which also leads to a stronger diffusion effect. Nevertheless, the overall propagation direction and dispersion regions remain well aligned with observations. In this paper, we will focus on the analysis of the volcanic SO<sub>2</sub> mass evolution and chemical lifetime based on this baseline simulation.

### 3.2 SO<sub>2</sub> chemical lifetime analysis

The time evolution of the total SO<sub>2</sub> mass burden of the 2019 Raikoke eruption from the MPTRAC simulations and TROPOMI observations is shown in Fig. 5a. The total mass burdens from the model and the observations were obtained by integrating the SO<sub>2</sub> column densities on a  $0.1^\circ \times 0.1^\circ$  horizontal grid. For this comparison, the satellite data and the grid output of the model were sampled with a lower detection limit of 0.35 DU and weighted by the mean kernel function of the TROPOMI observations to reduce the impact of noise and other uncertainties and to account for the vertical sensitivity of the measurements. It is found that the SO<sub>2</sub> lifetime modeled with the implicit KPP solution is about 1.6 times larger than that of the simplified explicit approximation. This can also be seen from a comparison of the vertical profiles of the  $e$ -folding lifetimes in Fig. 6.

The lifetime profile obtained with the KPP implicit solution indicates that the SO<sub>2</sub> has much longer lifetimes at higher altitudes. The lifetime is typically within a few hours to several days below an altitude of 5 km, whereas it exceeds 10 to 100 d above an altitude of 5 km. Due to the frequent presence of clouds in the lower and middle troposphere, SO<sub>2</sub> is taken up into the liquid phase and decays rapidly due to cloud-phase oxidation with H<sub>2</sub>O<sub>2</sub> and wet deposition, leading to the shorter lifetime compared with the stratosphere. The vertical lifetime profile of the implicit KPP scheme shows a peak in the stratosphere that is not found

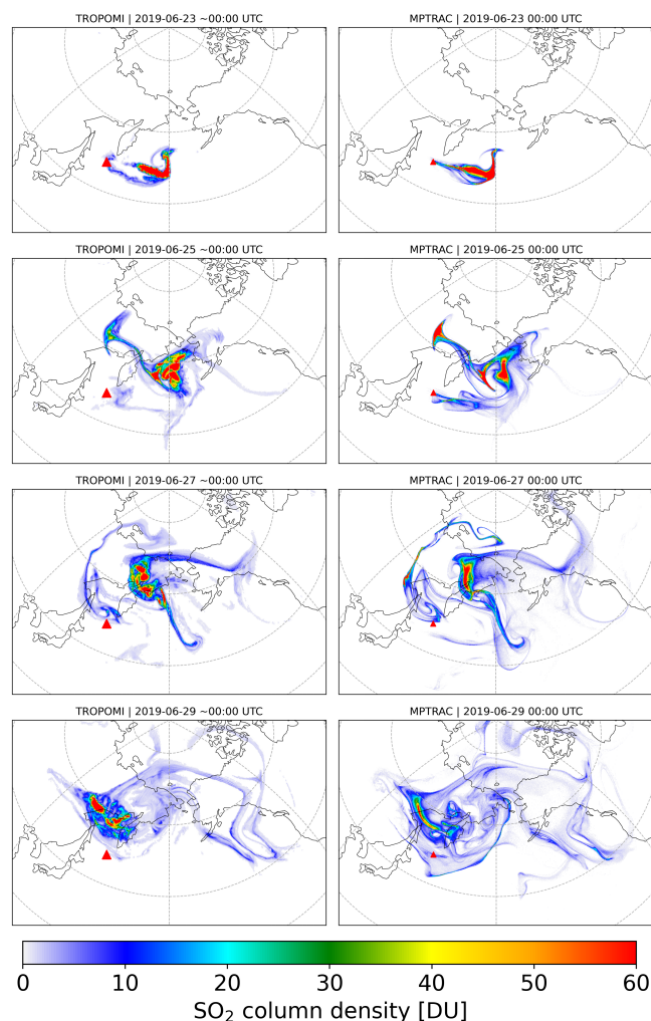


**Figure 3.** Evolution of SO<sub>2</sub> total column density distributions from 23 to 29 June 2019 from the MPTRAC simulation with the implicit chemistry scheme (right column) and the TROPOMI satellite observations (left column). The red triangle marks the location of the Raikoke volcano.

in the explicit scheme. This is attributed to a reduction in the OH concentration within the SO<sub>2</sub> plume, which is captured by the implicit chemistry scheme but not by the explicit scheme, which uses a constant OH climatology.

While still within the uncertainty range of the TROPOMI observations, Fig. 5a highlights a notable discrepancy between the SO<sub>2</sub> total mass from TROPOMI and the MPTRAC simulations during 3–15 July 2019. The work of de Leeuw et al. (2021) attributed the change in SO<sub>2</sub> lifetime observed by TROPOMI about 10 d after the eruption to the removal of a large fraction of the tropospheric SO<sub>2</sub> mass through aqueous-phase oxidation and wet deposition. Beyond this point, the TROPOMI observations become dominated by the stratospheric component of the SO<sub>2</sub> cloud. As the stratosphere contains much less moisture, SO<sub>2</sub> removal occurs at a much lower rate, primarily through gas-phase reactions with

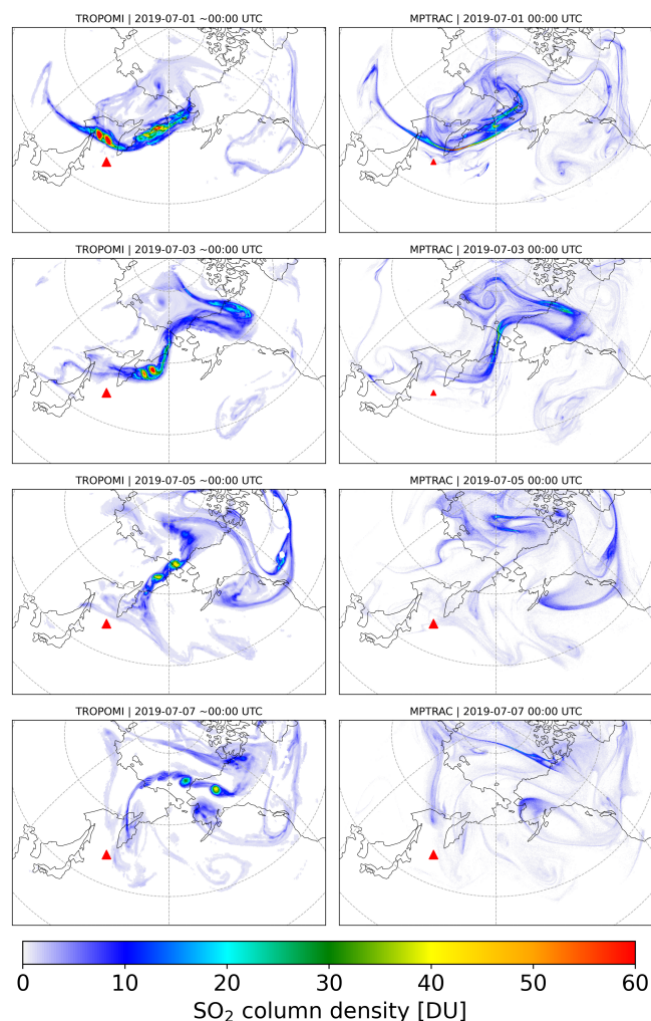


**Figure 4.** Same as Fig. 3 but from 1 to 7 July 2019.

OH, leading to significantly longer  $e$ -folding lifetimes. Our MPTRAC simulations are based on the SO<sub>2</sub> injection profiles provided by Cai et al. (2022), which may underestimate the stratospheric fraction and, consequently, impact on long-range transport. However, the estimates of SO<sub>2</sub> mass loss from the MPTRAC simulations (Fig. 5b) indicate a significant reduction in loss rates from wet deposition and H<sub>2</sub>O<sub>2</sub> oxidation after 3 July. This aligns closely with the findings of de Leeuw et al. (2021).

### 3.3 Correction for the simplified explicit scheme

From Figs. 5 and 6, it can be seen that the simplified explicit approximation overestimates the SO<sub>2</sub> decay rate by  $\sim 60\%$  compared with the TROPOMI observations, whereas the implicit KPP solution agrees well with the TROPOMI observations. Hence, there is also a  $\sim 60\%$  difference between the explicit solution and the KPP solution. This overestimation in the explicit scheme is likely due to changes in OH and

other radicals resulting from the SO<sub>2</sub> injection itself, which are not accounted for in the climatology. To account for that, we developed an SO<sub>2</sub>-dependent correction to the OH climatology. Essentially, the simplification of the explicit scheme applies a linear approximation to describe the nonlinear oxidation processes. To compare the differences in lifetime of the two schemes, we performed another simulation without SO<sub>2</sub> injections to estimate the undisturbed background levels of OH and H<sub>2</sub>O<sub>2</sub> and compared them with the conditions in the SO<sub>2</sub> plume. Figure 7 shows the ratio of the OH and H<sub>2</sub>O<sub>2</sub> concentrations in the SO<sub>2</sub> plume versus the background oxidant concentrations as a function of the SO<sub>2</sub> VMR. The ratio decreases as the abundance of SO<sub>2</sub> increases, which means that the depletion of the oxidants is faster than their production. In highly concentrated SO<sub>2</sub> regions, the oxidants are almost completely depleted.

Note that the data points shown in Fig. 7 are filtered using a  $z$ -score threshold, as there are factors other than the chemical reactions that will affect the SO<sub>2</sub> distributions, such as diffusion, convection, and wet deposition, causing the data not to be statistically representative. After filtering outliers with low  $z$  scores, a correction formula to estimate OH concentrations in the plume from OH background levels and the SO<sub>2</sub> concentration can be obtained by regression:

$$[\text{OH}] = 4.72 \times 10^{-8} [\text{SO}_2]^{-0.83} \times [\text{OH}]_{\text{background}}. \quad (3)$$

Similarly, the correction formula for H<sub>2</sub>O<sub>2</sub> is

$$[\text{H}_2\text{O}_2] = 3.13 \times 10^{-6} [\text{SO}_2]^{-0.57} \times [\text{H}_2\text{O}_2]_{\text{background}}. \quad (4)$$

By applying the corrections to the climatological OH and H<sub>2</sub>O<sub>2</sub> data to account for their removal in the SO<sub>2</sub> plume, a simulation with the simplified explicit approximation with correction can be conducted. Figure 6 shows that, above an altitude of 10 km, the correction for the simplified explicit solution shifts the simulated lifetime closer to the KPP implicit solution. The correction reduces the amount of the oxidants when SO<sub>2</sub> is highly abundant in the volcanic plume. The mass evolution simulated by the corrected explicit solution is, therefore, in better agreement with the TROPOMI measurements and the KPP implicit solution (Fig. 5). These results reflect the fact that the chemical degradation of volcanic SO<sub>2</sub> is a nonlinear process, which means that it should not simply be treated as a pseudo-first-order reaction. The correction of the OH and H<sub>2</sub>O<sub>2</sub> concentrations applied to the explicit solution improves the representation of SO<sub>2</sub> decay in the chemistry transport simulations, with almost no additional computational overhead.

### 3.4 Evaluation of the simulated OH field

The hydroxyl radical (OH) is an important oxidant in atmospheric chemistry, controlling the chemical decomposition of various species. For chemistry transport simulations of volcanic SO<sub>2</sub> in the UT–LS region, oxidation via OH is the main

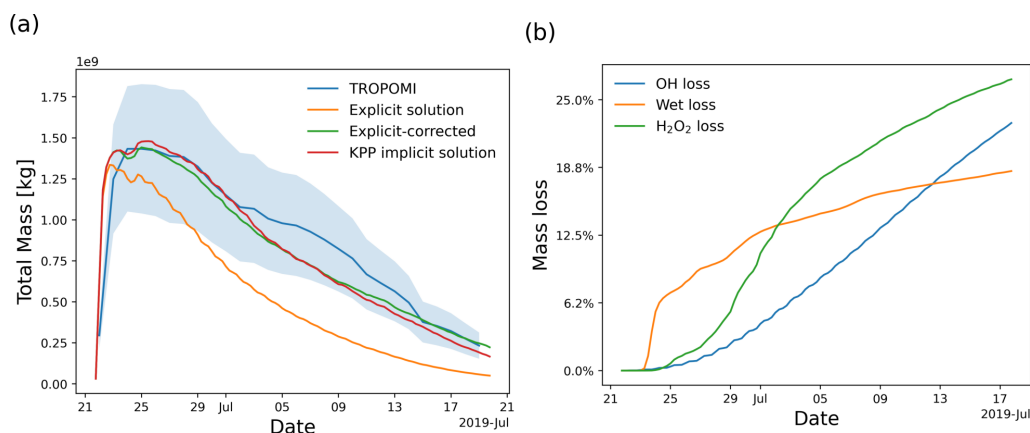


**Figure 5.** (a) Temporal evolution of the SO<sub>2</sub> total mass burden of the 2019 Raikoke eruption from TROPOMI measurements (blue curve, with the shading showing the uncertainty range) and MPTRAC simulations with the explicit solution (orange curve), the simplified explicit solution with correction (green curve), and the KPP implicit solution (red curve). (b) Estimates of the SO<sub>2</sub> total mass loss of the Raikoke eruption due to OH oxidation (blue curve), wet deposition (orange curve), and H<sub>2</sub>O<sub>2</sub> oxidation (green curve) from the simplified explicit solution with correction.

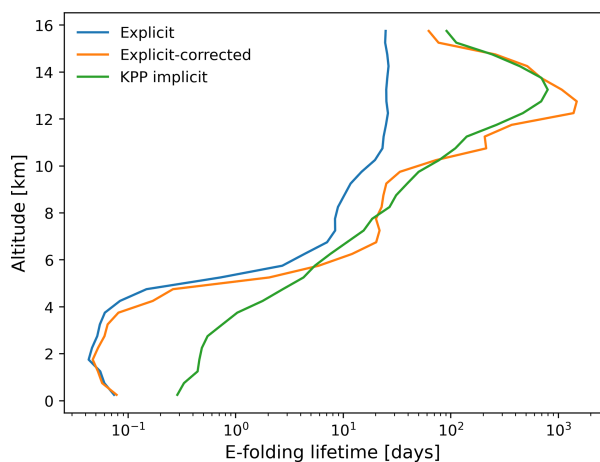


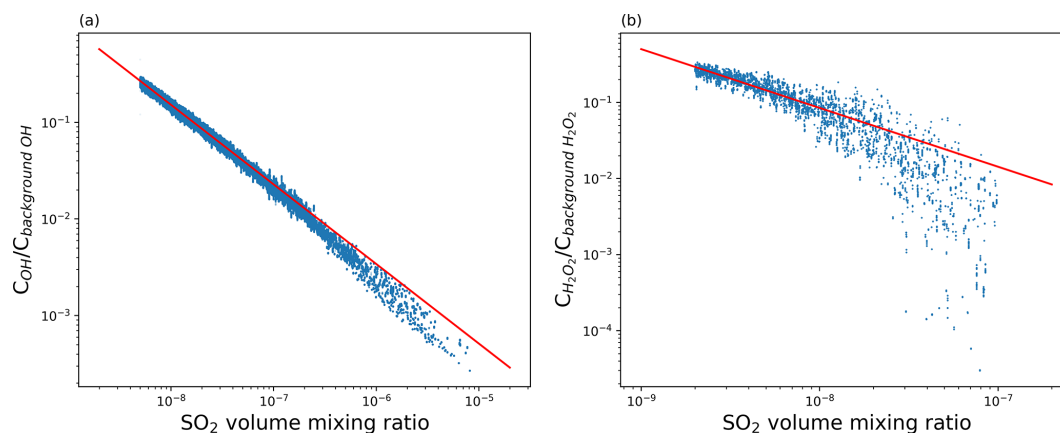
**Figure 6.** Vertical profiles of the average SO<sub>2</sub> *e*-folding lifetime of MPTRAC simulations with the explicit solution (green curve), the explicit solution with correction (orange curve), and the KPP implicit solution (blue curve) during the period from 25 June to 4 July.

factor of mass decay in the gas phase. In order to simulate the OH background conditions during the Raikoke case study without any enhanced levels of volcanic SO<sub>2</sub> abundance with the chemical mechanism introduced in Sect. 2.2.2, we distributed a total of 1 million air parcels at altitudes between 9 and 17 km. The fourth-generation Copernicus Atmosphere Monitoring Service (CAMS) global reanalysis data (Inness et al., 2019) were then used for comparison with the OH field obtained with the implicit chemistry scheme implemented in MPTRAC. The CAMS reanalysis combines model data with observations using data assimilation techniques, providing a global distribution of atmospheric species. Key species assimilated in the CAMS reanalysis include ozone (O<sub>3</sub>), carbon

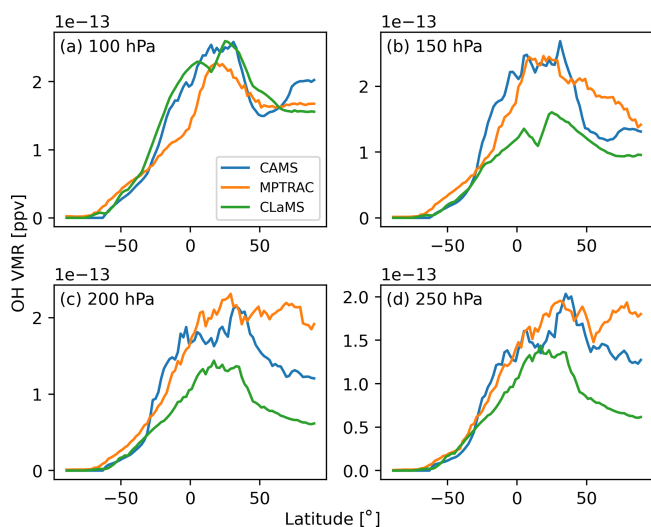
monoxide (CO), nitrogen dioxide (NO<sub>2</sub>), methane (CH<sub>4</sub>), and carbon dioxide (CO<sub>2</sub>). Note that the hydroxyl radical (OH) and hydrogen peroxide (H<sub>2</sub>O<sub>2</sub>) are not directly assimilated from observations; instead, their concentrations are computed using the chemistry scheme implemented in the CAMS reanalysis.

Figure 8 compares zonal mean OH distributions at different pressure levels from the CAMS reanalysis, the MPTRAC model, and the CLaMS climatology. The best agreement among the three datasets is observed at the 100 hPa pressure level. Zonal mean OH concentrations increase gradually from near zero under polar winter conditions at high southern latitudes to approximately  $2.5 \times 10^{-13}$  ppv (parts per volume) in the northern subtropics. At northern middle and high latitudes, OH concentrations remain within 1.5 to  $2 \times 10^{-13}$  ppv. At lower vertical levels (150 to 250 hPa), differences of up to a factor of 2 are observed in the tropics and at northern middle to high latitudes. Overall, the CAMS and MPTRAC datasets tend to agree more closely with each other than with the CLaMS data. Differences in OH concentrations arise from variations in chemical mechanisms, emissions, meteorological conditions, photolysis schemes, spatial resolution, boundary conditions, and the representation of stratosphere–troposphere exchange processes.

Figure 9 shows the global CAMS and MPTRAC OH fields at pressure levels of 100 to 250 hPa at 00:00 UTC on 1 July 2019. The OH fields obtained by MPTRAC were generated using its implicit chemistry scheme under SO<sub>2</sub>-free conditions. The MPTRAC OH fields exhibit similar spatial distributions with respect to the solar zenith angle dependence to the CAMS data, reflecting the strong correlation between OH production and solar radiation. The magnitudes of the OH concentrations produced by the two models are compa-



**Figure 7.** Ratio of the OH concentration in dry atmosphere (a) and the H<sub>2</sub>O<sub>2</sub> concentration in cloud regions (b) in the Raikoke SO<sub>2</sub> plume versus background levels as a function of the SO<sub>2</sub> VMR. Each data point represents a single air parcel. The red lines represent the regression formulas given in Eqs. (3) and (4).



**Figure 8.** Zonal mean distributions of the OH field obtained from the CAMS reanalysis (blue curves), climatological data from the CLaMS model (green curves), and the MPTRAC simulation (orange curves) at pressure levels of 100 hPa (a), 150 hPa (b), 200 hPa (c), and 250 hPa (d) at 00:00 UTC on 1 July 2019.

able, underscoring the reliability of MPTRAC with respect to capturing key OH dynamics.

A closer inspection reveals distinct features in the CAMS OH fields that are absent in the MPTRAC fields, such as localized OH plumes over Japan and the Pacific visible in the CAMS data. This discrepancy likely stems from the simplified oxidant mechanisms used in MPTRAC, which smooth out regional OH enhancements captured by CAMS. Additional factors, such as differences in spatial and temporal resolution and the representation of regional emissions and environmental conditions, further contribute to the observed differences. Despite these limitations, the MPTRAC scheme

demonstrates a reasonable ability to simulate the production and loss of the short-lived OH radical in the UT–LS region, offering a practical balance between accuracy and computational efficiency for modeling SO<sub>2</sub> lifetimes in volcanic plumes and other atmospheric scenarios.

### 3.5 Selection of the chemistry time step

In MPTRAC, a fixed time step is applied for numerical integration of the trajectories and in most other modules. Based on previous studies (Röbler et al., 2018; Clemens et al., 2024), a time step of 180 s was selected for calculating trajectories with the midpoint method and considering the spatiotemporal resolution of the ERA5 reanalysis data. This choice of the time step provides a reasonable trade-off in terms of accuracy and the computational cost of the trajectory calculations (i.e., it is small enough to consider integration errors negligible while providing a minimum in computation time). In terms of computation effort, the time step of 180 s is acceptable for the explicit solution, but it is not efficient for the implicit chemistry calculations, which is particularly demanding in terms of computation.

To improve the computational efficiency for the implicit chemistry scheme, we implemented a distinct time step for the chemistry calculations. The chemistry time step is an important control parameter, as it has a significant impact on the computational efficiency. The chemistry time step size should be as large as possible without compromising the accuracy of the results. Figure 10 shows the temporal evolution of the SO<sub>2</sub> total mass obtained by different chemistry time steps. The results diverge when the time step of the chemistry calculations is larger than 6 h. Therefore, we recommend using a chemistry time step of 3 to 6 h to balance the computational efficiency and accuracy of the solution for the volcanic SO<sub>2</sub> oxidation.

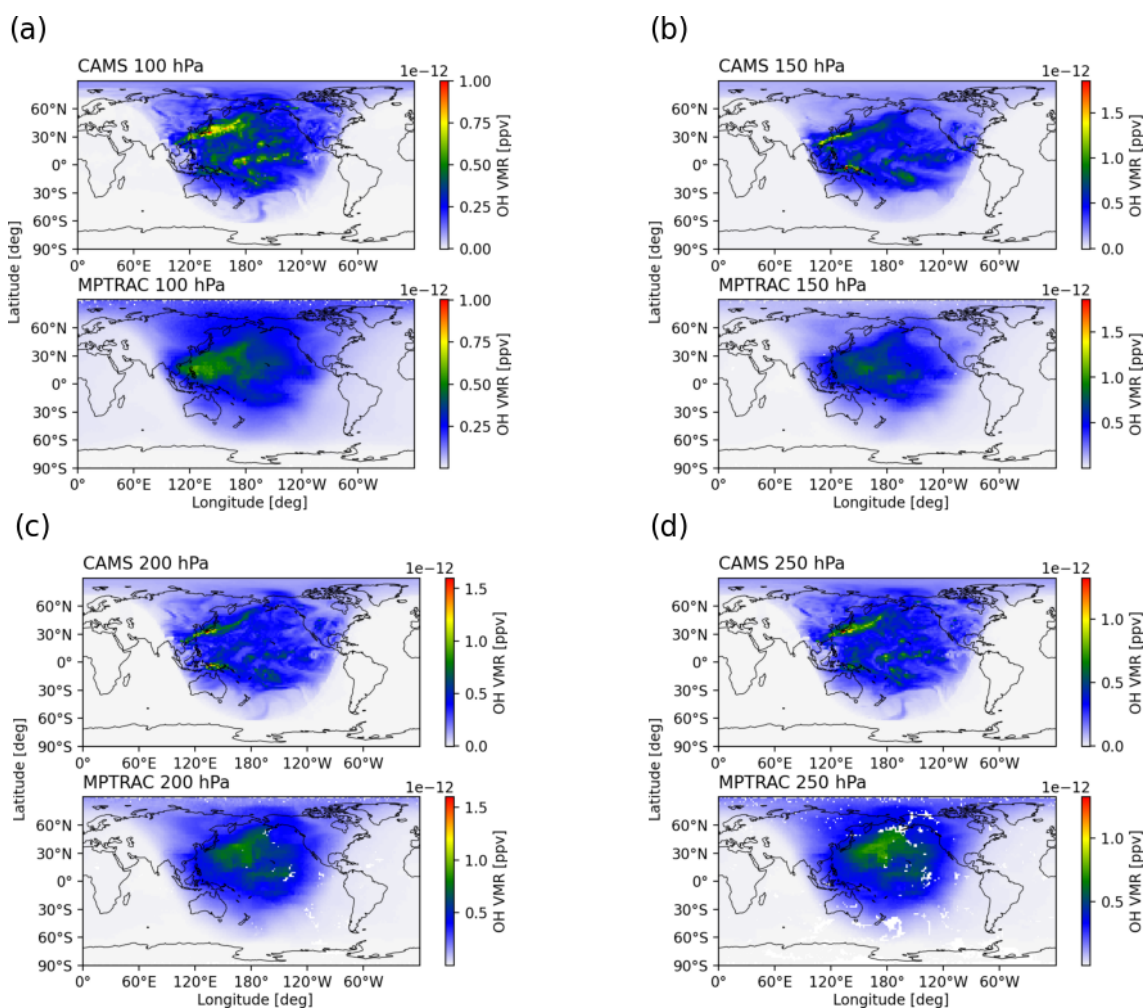


**Figure 9.** Global OH fields obtained from the CAMS reanalysis (top) and MPTRAC simulations (bottom) at pressure levels of 100 hPa (a), 150 hPa (b), 200 hPa (c), and 250 hPa (d) at 00:00 UTC on 1 July 2019.

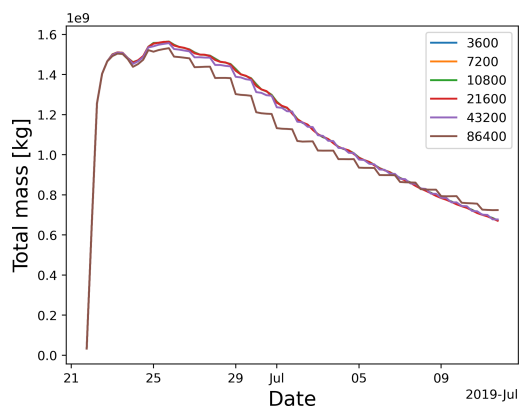


**Figure 10.** Total mass burden evolution simulated with different chemistry time step size settings of 3600, 7200, 10 800, 21 600, 43 200, and 86 400 s (see the legend).

### 3.6 Assessment of computational costs

The KPP-based implicit chemistry solver implemented in MPTRAC can solve complex chemical mechanisms with a flexible definition of the chemical reactions and species. In the case of the volcanic SO<sub>2</sub> chemistry transport simulations, the corrected explicit solution achieves similar results with higher computational efficiency. For now, GPU offloading has been implemented using OpenACC for the simplified explicit scheme, whereas this is planned for the future for the implicit scheme. Figure 11 shows the runtime of MPTRAC simulations on the JUWELS supercomputer at the Jülich Supercomputing Centre comparing the implicit and explicit chemistry schemes using a chemistry time step of 21 600 and 180 s, respectively. The CPU simulations were conducted on a single compute node of the JUWELS Cluster (Jülich Supercomputing Centre, 2019), parallelized with 48 OpenMP threads. Each compute node of the JUWELS Cluster contains two Intel Xeon Platinum 8168 CPUs with

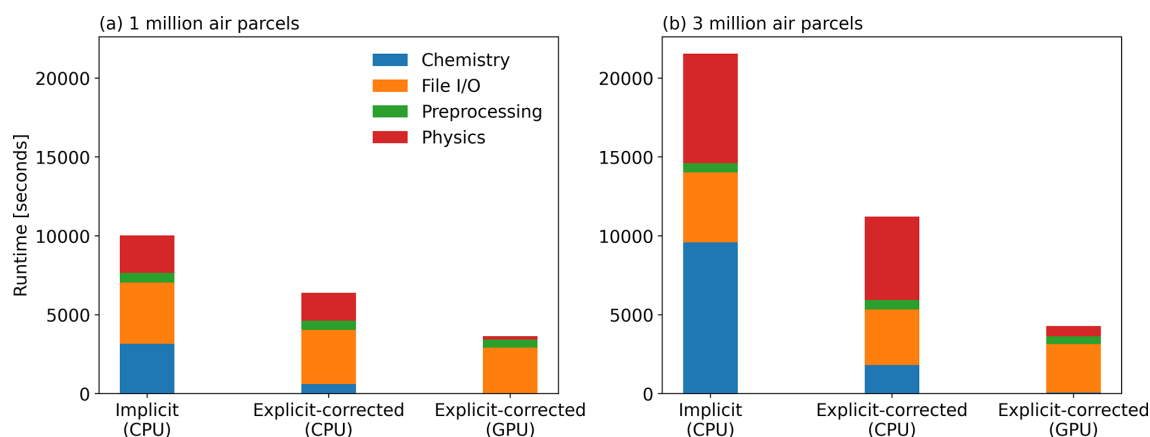


**Figure 11.** Computational cost of the Raikoke simulations with different chemistry schemes (the implicit scheme and the simplified explicit scheme with correction) on the JUWELS Cluster (CPU) and JUWELS Booster (GPU) for a simulation with 1 million air parcels on a scale of 1 million air parcels (a) and 3 million air parcels (b). The blue bar represents the runtime for the chemistry calculations, whereas the red bar represents the runtime for the other physical modules besides chemistry.

24 physical cores per CPU. The GPU simulations were conducted on the JUWELS Booster (Jülich Supercomputing Centre, 2021) with two AMD EPYC Rome 7402 CPUs and four NVIDIA A100 GPUs per node.

Regarding the chemistry, Fig. 11a shows that the simplified explicit solution is about 5.3 times faster than the KPP implicit solution for a simulation with 1 million air parcels. Considering that file input/output (I/O) and meteorological data preprocessing also require a substantial part of the total runtime, the total runtime is reduced by  $\sim 56\%$  by choosing the more efficient explicit chemistry scheme. The GPU solution of the simplified explicit chemistry scheme on the JUWELS Booster reduces the total runtime by  $\sim 75\%$ , with the runtime required for chemistry becoming nearly negligible. As the scale of the simulation increases (i.e., for simulations with more air parcels), the advantage of the explicit solution in terms of computational efficiency becomes even more pronounced. Figure 11b shows that the total runtime is reduced by 92% for a simulation with 3 million air parcels. This improvement in computational efficiency is particularly relevant for large-scale chemistry transport simulations, where finding the proper trade-off between accuracy and computational cost is most critical. In the future, the KPP implicit scheme might also be equipped with GPU offloading to improve its performance (Alvanos and Christoudias, 2017; Christoudias et al., 2021).

#### 4 Summary and conclusions

The MPTRAC Lagrangian transport model offers two schemes for simulating SO<sub>2</sub> chemistry in volcanic eruptions: (1) an explicit approach utilizing climatological data for reaction rates and SO<sub>2</sub> decay and (2) an implicit approach leveraging KPP's Rosenbrock integrator for multi-species chemical processes. KPP can solve complex chemical mechanisms

with a flexible definition of chemical species, reactions, and rate coefficients. The implicit solution allows for more complex, nonlinear chemical mechanisms with dynamic reaction rates depending on the species concentrations. Here, we propose a chemical mechanism with 31 reactions and 12 species to model the production and loss of the short-lived OH radical and H<sub>2</sub>O<sub>2</sub>, which are essential for the decomposition of SO<sub>2</sub> in the gas and aqueous phase, respectively, in the UT–LS region. The mechanism proposed here can serve as a basis for developing more complex chemical mechanisms in future studies. It could also be further optimized by evaluating the relevance of each reaction pathway to reduce the computational effort.

The OH radical is the main oxidant in the gas phase, which largely controls the decomposition of SO<sub>2</sub> in the UT–LS. We compared OH radical fields obtained by the proposed mechanism in MPTRAC with CAMS reanalysis data and climatological data from the CLaMS model. The OH radical field obtained by the proposed mechanism shows a clear characteristic of diurnal variation and concentrations at a similar level compared to these reference datasets. The cloud-phase H<sub>2</sub>O<sub>2</sub> oxidation also has a significant impact on the SO<sub>2</sub> decay in the lower troposphere. It must be taken into account to properly represent the loss of tropospheric SO<sub>2</sub> over time, especially for other volcanic eruptions, such as those happening in the tropics with lower peak emission heights (Liu et al., 2023). Cloud-phase oxidation has been considered in all cases in this study.

Applying the chemical mechanisms to the June 2019 Raikoke eruption, the implicit KPP-based solution aligns well with TROPOMI satellite data on SO<sub>2</sub> mass burden evolution, whereas the simplified explicit approach overestimates SO<sub>2</sub> decay by 60%. This overestimation is due to using the OH and H<sub>2</sub>O<sub>2</sub> climatological background field without considering enhanced levels of SO<sub>2</sub>. Regression-

derived correction formulas for OH and H<sub>2</sub>O<sub>2</sub> concentrations ( $y = ax^b$ ) adjust climatology-based oxidant levels, introducing nonlinear effects that enhance SO<sub>2</sub> lifetime representation in explicit simulations. We also applied the correction to another volcanic eruption, the July 2018 Ambae eruption (Liu et al., 2023), and observed that it produced a total SO<sub>2</sub> lifetime comparable to that predicted by the KPP implicit solution. Notably, despite differences in the geographic and atmospheric condition – Ambae is situated in the tropics and Raikoke is located in the midlatitudes – the same parameter values for  $a$  and  $b$  in the correction formula were used. This suggests that the correction approach is transferable across diverse eruption scenarios.

The corrected explicit solution achieves realistic lifetime modeling with more than 5 times the efficiency of the implicit approach, making it ideal for computationally demanding applications, such as emission reconstruction through inverse modeling. Previous studies using backward-trajectory methods for volcanic SO<sub>2</sub> lacked realistic chemical lifetime modeling, a limitation now being addressed. Ongoing development includes inverse modeling techniques for source estimation, incorporating support for nonlinear chemical mechanisms, and investigating the interplay between lifetime modeling and source reconstruction. These advancements significantly enhance MPTRAC's Lagrangian chemistry modeling capabilities, enabling more precise source estimation and positioning the model for broader applications on modern HPC systems.

**Code and data availability.** The MPTRAC model (Hoffmann et al., 2016, 2022) is distributed under the terms and conditions of the GNU General Public License (GPL) version 3. The version 2.7 release of MPTRAC used in this paper is archived on Zenodo (<https://doi.org/10.5281/zenodo.12751121>, Hoffmann et al., 2024a). Newer versions of MPTRAC are available from the repository at <https://github.com/slcs-jsc/mptrac> (last access: 3 December 2024). The ERA5 data were obtained from the European Centre for Medium-Range Weather Forecasts (see <https://doi.org/10.24381/cds.bd0915c6>, Hersbach et al., 2023). The TROPOMI data are provided at <https://doi.org/10.5270/S5P-74eidii> (European Space Agency, 2025).

**Author contributions.** ML and LH: conceptualization; LH, SG, JUG, and ZC: data curation; ML: formal analysis; LH, JUG, and YH: methodology; ML and LH: software; LH: supervision; ML: validation; ML and LH: writing – original draft; ML, LH, SG, JUG, ZC, and YH: writing – review and editing.

**Competing interests.** At least one of the (co-)authors is a member of the editorial board of *Atmospheric Chemistry and Physics*. The peer-review process was guided by an independent editor, and the authors also have no other competing interests to declare.

**Disclaimer.** Publisher's note: Copernicus Publications remains neutral with regard to jurisdictional claims made in the text, published maps, institutional affiliations, or any other geographical representation in this paper. While Copernicus Publications makes every effort to include appropriate place names, the final responsibility lies with the authors.

**Acknowledgements.** This research was supported by the Helmholtz Association of German Research Centres (HGF) through the Joint Laboratory for Exascale Earth System Modeling (JL-ExaESM). The authors are grateful to the Jülich Supercomputing Center for providing computing time and storage resources on the JUWELS supercomputer. We acknowledge the use of the AI tool DeepL for language editing of the original manuscript.

**Financial support.** The article processing charges for this open-access publication were covered by the Forschungszentrum Jülich.

**Review statement.** This paper was edited by Matthew Toohey and reviewed by two anonymous referees.

## References

- Alvanos, M. and Christoudias, T.: GPU-accelerated atmospheric chemical kinetics in the ECHAM/MESSy (EMAC) Earth system model (version 2.52), *Geosci. Model Dev.*, 10, 3679–3693, <https://doi.org/10.5194/gmd-10-3679-2017>, 2017.
- Becker, G., Grooß, J.-U., McKenna, D. S., and Müller, R.: Stratospheric photolysis frequencies: Impact of an improved numerical solution of the radiative transfer equation, *J. Atmos. Chem.*, 37, 217–229, <https://doi.org/10.1023/A:1006468926530>, 2000.
- Bergamaschi, P., Segers, A., Brunner, D., Haussaire, J.-M., Henne, S., Ramonet, M., Arnold, T., Biermann, T., Chen, H., Conil, S., Delmotte, M., Forster, G., Frumau, A., Kubistin, D., Lan, X., Leuenberger, M., Lindauer, M., Lopez, M., Manca, G., Müller-Williams, J., O'Doherty, S., Scheeren, B., Steinbacher, M., Trisolino, P., Vítková, G., and Yver Kwok, C.: High-resolution inverse modelling of European CH<sub>4</sub> emissions using the novel FLEXPART-COSMO TM5 4DVAR inverse modelling system, *Atmos. Chem. Phys.*, 22, 13243–13268, <https://doi.org/10.5194/acp-22-13243-2022>, 2022.
- Brunner, D.: Atmospheric Chemistry in Lagrangian Models—Overview, Chap. 19, *American Geophysical Union (AGU)*, ISBN 9781118704578, 224–234, <https://doi.org/10.1029/2012GM001431>, 2012.
- Brunner, D., Arnold, T., Henne, S., Manning, A., Thompson, R. L., Maione, M., O'Doherty, S., and Reimann, S.: Comparison of four inverse modelling systems applied to the estimation of HFC-125, HFC-134a, and SF<sub>6</sub> emissions over Europe, *Atmos. Chem. Phys.*, 17, 10651–10674, <https://doi.org/10.5194/acp-17-10651-2017>, 2017.
- Burkholder, J. B., Sander, S. P., J. Abbatt, J. R. B., Cappa, C., Crounse, J. D., Dibble, T. S., Huie, R. E., Kolb, C. E., Kurylo, M. J., Orkin, V. L., Percival, C. J., Wilmouth, D. M., and Wine, P. H.: Chemical kinetics and photochemical data for use in at-

- ospheric studies: evaluation number 19, Tech. rep., Jet Propulsion Laboratory, Pasadena, <https://jpldataeval.jpl.nasa.gov/> (last access: 25 March 2025), 2019.
- Cai, Z., Griessbach, S., and Hoffmann, L.: Improved estimation of volcanic SO<sub>2</sub> injections from satellite retrievals and Lagrangian transport simulations: the 2019 Raikoke eruption, *Atmos. Chem. Phys.*, 22, 6787–6809, <https://doi.org/10.5194/acp-22-6787-2022>, 2022.
- Che, K., Cai, Z., Liu, Y., Wu, L., Yang, D., Chen, Y., Meng, X., Zhou, M., Wang, J., Yao, L., and Wang, P.: Lagrangian inversion of anthropogenic CO<sub>2</sub> emissions from Beijing using differential column measurements, *Environ. Res. Lett.*, 17, 075001, <https://doi.org/10.1088/1748-9326/ac7477>, 2022.
- Christoudias, T., Kirfel, T., Kerkweg, A., Taraborrelli, D., Moulard, G.-E., Raffin, E., Azizi, V., Oord, G. V. D., and Werkhoven, B. V.: GPU Optimizations for Atmospheric Chemical Kinetics, in: HPCAsia '21: The International Conference on High Performance Computing in Asia-Pacific Region, Virtual Event, Republic of Korea, 20–22 January 2021, Association for Computing Machinery, New York, NY, USA, 136–138, <https://doi.org/10.1145/3432261.3439863>, 2021.
- Clemens, J., Hoffmann, L., Vogel, B., Griebbach, S., and Thomas, N.: Implementation and evaluation of diabatic advection in the Lagrangian transport model MPTRAC 2.6, *Geosci. Model Dev.*, 17, 4467–4493, <https://doi.org/10.5194/gmd-17-4467-2024>, 2024.
- Collins, W., Johnson, C., and Derwent, R.: Tropospheric Ozone in a Global-Scale Three-Dimensional Lagrangian Model and Its Response to NO<sub>x</sub> Emission Controls, *J. Atmos. Chem.*, 26, 223–274, <https://doi.org/10.1023/A:1005836531979>, 1997.
- Dalsøren, S. B., Myhre, G., Hodnebrog, Ø., Myhre, C. L., Stohl, A., Pisso, I., Schwietzke, S., Höglund-Isaksson, L., Helmig, D., Reimann, S., Sauvage, S., Schmidbauer, N., Read, K. A., Carpenter, L. J., Lewis, A. C., Punjabi, S., and Wallasch, M.: Discrepancy between simulated and observed ethane and propane levels explained by underestimated fossil emissions, *Nat. Geosci.*, 11, 178–184, <https://doi.org/10.1038/s41561-018-0073-0>, 2018.
- Damian, V., Sandu, A., Damian, M., Potra, F., and Carmichael, G. R.: The kinetic preprocessor KPP—a software environment for solving chemical kinetics, *Comput. Chem. Eng.*, 26, 1567–1579, [https://doi.org/10.1016/S0098-1354\(02\)00128-X](https://doi.org/10.1016/S0098-1354(02)00128-X), 2002.
- Dee, D. P., Uppala, S. M., Simmons, A. J., Berrisford, P., Poli, P., Kobayashi, S., Andrae, U., Balmaseda, M. A., Balsamo, G., Bauer, P., Bechtold, P., Beljaars, A. C. M., van de Berg, L., Bidlot, J., Bormann, N., Delsol, C., Dragani, R., Fuentes, M., Geer, A. J., Haimberger, L., Healy, S. B., Hersbach, H., Hólm, E. V., Isaksen, I., Kållberg, P., Köhler, M., Matricardi, M., McNally, A. P., Monge-Sanz, B. M., Morcrette, J.-J., Park, B.-K., Peubey, C., de Rosnay, P., Tavolato, C., Thépaut, J.-N., and Vitart, F.: The ERA-Interim reanalysis: configuration and performance of the data assimilation system, *Q. J. Roy. Meteor. Soc.*, 137, 553–597, <https://doi.org/10.1002/qj.828>, 2011.
- de Leeuw, J., Schmidt, A., Witham, C. S., Theys, N., Taylor, I. A., Grainger, R. G., Pope, R. J., Haywood, J., Osborne, M., and Kristiansen, N. I.: The 2019 Raikoke volcanic eruption – Part 1: Dispersion model simulations and satellite retrievals of volcanic sulfur dioxide, *Atmos. Chem. Phys.*, 21, 10851–10879, <https://doi.org/10.5194/acp-21-10851-2021>, 2021.
- European Space Agency (ESA): Sentinel-5P Level 2 Data Products Documentation, ESA, <https://doi.org/10.5270/SSP-74eidii>, last access: 28 March 2025.
- Evangelou, N., Kylling, A., Eckhardt, S., Myroniuk, V., Stebel, K., Paugam, R., Zibitsev, S., and Stohl, A.: Open fires in Greenland in summer 2017: transport, deposition and radiative effects of BC, OC and BrC emissions, *Atmos. Chem. Phys.*, 19, 1393–1411, <https://doi.org/10.5194/acp-19-1393-2019>, 2019.
- Gerbig, C., Lin, J. C., Wofsy, S. C., Daube, B. C., Andrews, A. E., Stephens, B. B., Bakwin, P. S., and Grainger, C. A.: Toward constraining regional-scale fluxes of CO<sub>2</sub> with atmospheric observations over a continent: 2. Analysis of COBRA data using a receptor-oriented framework, *J. Geophys. Res.*, 108, 4757, <https://doi.org/10.1029/2003JD003770>, 2003.
- Gorkavyi, N., Krotkov, N., Li, C., Lait, L., Colarco, P., Carn, S., DeLand, M., Newman, P., Schoeberl, M., Taha, G., Torres, O., Vasilkov, A., and Joiner, J.: Tracking aerosols and SO<sub>2</sub> clouds from the Raikoke eruption: 3D view from satellite observations, *Atmos. Meas. Tech.*, 14, 7545–7563, <https://doi.org/10.5194/amt-14-7545-2021>, 2021.
- Heng, Y., Hoffmann, L., Griessbach, S., Rößler, T., and Stein, O.: Inverse transport modeling of volcanic sulfur dioxide emissions using large-scale simulations, *Geosci. Model Dev.*, 9, 1627–1645, <https://doi.org/10.5194/gmd-9-1627-2016>, 2016.
- Henze, D. K., Hakami, A., and Seinfeld, J. H.: Development of the adjoint of GEOS-Chem, *Atmos. Chem. Phys.*, 7, 2413–2433, <https://doi.org/10.5194/acp-7-2413-2007>, 2007.
- Hersbach, H., Bell, B., Berrisford, P., Hirahara, S., Horanyi, A., Muñoz-Sabater, J., Nicolas, J., Peubey, C., Radu, R., Schepers, D., Simmons, A., Soci, C., Abdalla, S., Abellan, X., Balsamo, G., Bechtold, P., Biavati, G., Bidlot, J., Bonavita, M., De Chiara, G., Dahlgren, P., Dee, D., Diamantakis, M., Dragani, R., Flemming, J., Forbes, R., Fuentes, M., Geer, A., Haimberger, L., Healy, S., Hogan, R. J., Holm, E., Janiskova, M., Keeley, S., Laloyaux, P., Lopez, P., Lupu, C., Radnoti, G., de Rosnay, P., Rozum, I., Vamborg, F., Villaume, S., and Thepaut, J.-N.: The ERA5 global reanalysis, *Q. J. Roy. Meteor. Soc.*, 146, 1999–2049, <https://doi.org/10.1002/qj.3803>, 2020.
- Hersbach, H., Bell, B., Berrisford, P., Biavati, G., Horányi, A., Muñoz Sabater, J., Nicolas, J., Peubey, C., Radu, R., Rozum, I., Schepers, D., Simmons, A., Soci, C., Dee, D., and Thépaut, J.-N.: ERA5 hourly data on pressure levels from 1940 to present, Copernicus Climate Change Service (C3S) Climate Data Store (CDS) [data set], <https://doi.org/10.24381/cds.bd0915c6>, 2023.
- Hoffmann, L., Roessler, T., Griessbach, S., Heng, Y., and Stein, O.: Lagrangian transport simulations of volcanic sulfur dioxide emissions: Impact of meteorological data products, *J. Geophys. Res.*, 121, 4651–4673, <https://doi.org/10.1002/2015JD023749>, 2016.
- Hoffmann, L., Günther, G., Li, D., Stein, O., Wu, X., Griessbach, S., Heng, Y., Konopka, P., Müller, R., Vogel, B., and Wright, J. S.: From ERA-Interim to ERA5: the considerable impact of ECMWF's next-generation reanalysis on Lagrangian transport simulations, *Atmos. Chem. Phys.*, 19, 3097–3124, <https://doi.org/10.5194/acp-19-3097-2019>, 2019.
- Hoffmann, L., Baumeister, P. F., Cai, Z., Clemens, J., Griessbach, S., Günther, G., Heng, Y., Liu, M., Haghghi Mood, K., Stein, O., Thomas, N., Vogel, B., Wu, X., and Zou, L.: Massive-Parallel Trajectory Calculations version 2.2 (MPTRAC-

- 2.2): Lagrangian transport simulations on graphics processing units (GPUs), *Geosci. Model Dev.*, 15, 2731–2762, <https://doi.org/10.5194/gmd-15-2731-2022>, 2022.
- Hoffmann, L., Konopka, P., Clemens, J., and Vogel, B.: Lagrangian transport simulations using the extreme convection parameterization: an assessment for the ECMWF reanalyses, *Atmos. Chem. Phys.*, 23, 7589–7609, <https://doi.org/10.5194/acp-23-7589-2023>, 2023.
- Hoffmann, L., Clemens, J., Griessbach, S., Haghghi Mood, K., Khosrawi, F., Liu, M., Lu, Y.-S., Sonnabend, J., and Zou, L.: Massive-Parallel Trajectory Calculations (MPTRAC) v2.7, Zenodo [code], <https://doi.org/10.5281/zenodo.12751121>, 2024a.
- Hoffmann, L., Haghghi Mood, K., Herten, A., Hrywniak, M., Kraus, J., Clemens, J., and Liu, M.: Accelerating Lagrangian transport simulations on graphics processing units: performance optimizations of Massive-Parallel Trajectory Calculations (MPTRAC) v2.6, *Geosci. Model Dev.*, 17, 4077–4094, <https://doi.org/10.5194/gmd-17-4077-2024>, 2024b.
- Hoppe, C. M., Hoffmann, L., Konopka, P., Grooß, J.-U., Ploeger, F., Günther, G., Jöckel, P., and Müller, R.: The implementation of the CLaMS Lagrangian transport core into the chemistry climate model EMAC 2.40.1: application on age of air and transport of long-lived trace species, *Geosci. Model Dev.*, 7, 2639–2651, <https://doi.org/10.5194/gmd-7-2639-2014>, 2014.
- Inness, A., Ades, M., Agustí-Panareda, A., Barré, J., Benedictow, A., Blechschmidt, A.-M., Dominguez, J. J., Engelen, R., Eskes, H., Flemming, J., Huijnen, V., Jones, L., Kipling, Z., Massart, S., Parrington, M., Peuch, V.-H., Razinger, M., Remy, S., Schulz, M., and Suttie, M.: The CAMS reanalysis of atmospheric composition, *Atmos. Chem. Phys.*, 19, 3515–3556, <https://doi.org/10.5194/acp-19-3515-2019>, 2019.
- Jülich Supercomputing Centre: JUWELS: Modular Tier-0/1 Supercomputer at the Jülich Supercomputing Centre, *J. Large-scale Res. Facilities*, 5, A135, <https://doi.org/10.17815/jlsrf-5-171>, 2019.
- Jülich Supercomputing Centre: JUWELS Cluster and Booster: Exascale Pathfinder with Modular Supercomputing Architecture at Jülich Supercomputing Centre, *J. Large-scale Res. Facilities*, 7, A183, <https://doi.org/10.17815/jlsrf-7-183>, 2021.
- Kloss, C., Berthet, G., Sellitto, P., Ploeger, F., Taha, G., Tidiga, M., Eremenko, M., Bossolasco, A., Jégou, F., Renard, J.-B., and Legras, B.: Stratospheric aerosol layer perturbation caused by the 2019 Raikoke and Ulawun eruptions and their radiative forcing, *Atmos. Chem. Phys.*, 21, 535–560, <https://doi.org/10.5194/acp-21-535-2021>, 2021.
- Lary, D. J. and Pyle, J. A.: Diffuse radiation, twilight, and photochemistry – I, *J. Atmos. Chem.*, 13, 373–392, <https://doi.org/10.1007/BF00057753>, 1991.
- Liu, M., Huang, Y., Hoffmann, L., Huang, C., Chen, P., and Heng, Y.: High-Resolution Source Estimation of Volcanic Sulfur Dioxide Emissions Using Large-Scale Transport Simulations, in: *Computational Science – ICCS 2020*, edited by: Krzhizhanovskaya, V. V., Závodszky, G., Lees, M. H., Dongarra, J. J., Sliot, P. M. A., Brissos, S., and Teixeira, J., Springer International Publishing, 60–73, [https://doi.org/10.1007/978-3-030-50420-5\\_5](https://doi.org/10.1007/978-3-030-50420-5_5), 2020.
- Liu, M., Hoffmann, L., Griessbach, S., Cai, Z., Heng, Y., and Wu, X.: Improved representation of volcanic sulfur dioxide depletion in Lagrangian transport simulations: a case study with MPTRAC v2.4, *Geosci. Model Dev.*, 16, 5197–5217, <https://doi.org/10.5194/gmd-16-5197-2023>, 2023.
- McKenna, D. S., Grooß, J.-U., Günther, G., Konopka, P., Müller, R., Carver, G., and Sasano, Y.: A new Chemical Lagrangian Model of the Stratosphere (CLaMS) 2. Formulation of chemistry scheme and initialization, *J. Geophys. Res.*, 107, ACH 4-1–ACH 4-14, <https://doi.org/10.1029/2000JD000113>, 2002a.
- McKenna, D. S., Konopka, P., Grooß, J.-U., Günther, G., Müller, R., Spang, R., Offermann, D., and Orsolini, Y.: A new Chemical Lagrangian Model of the Stratosphere (CLaMS) 1. Formulation of advection and mixing, *J. Geophys. Res.*, 107, ACH 15-1–ACH 15-15, <https://doi.org/10.1029/2000JD000114>, 2002b.
- Minschwaner, K., Manney, G. L., Wang, S. H., and Harwood, R. S.: Hydroxyl in the stratosphere and mesosphere – Part I: Diurnal variability, *Atmos. Chem. Phys.*, 11, 955–962, <https://doi.org/10.5194/acp-11-955-2011>, 2011.
- Pardini, F., Burton, M., de’ Michieli Vitturi, M., Corradini, S., Salerno, G., Merucci, L., and Di Grazia, G.: Retrieval and intercomparison of volcanic SO<sub>2</sub> injection height and eruption time from satellite maps and ground-based observations, *J. Volcanol. Geoth. Res.*, 331, 79–91, <https://doi.org/10.1016/j.jvolgeores.2016.12.008>, 2017.
- Pattantyus, A. K., Businger, S., and Howell, S. G.: Review of sulfur dioxide to sulfate aerosol chemistry at Kilauea Volcano, Hawai’i, *Atmos. Environ.*, 185, 262–271, <https://doi.org/10.1016/j.atmosenv.2018.04.055>, 2018.
- Pommrich, R., Müller, R., Grooß, J.-U., Konopka, P., Ploeger, F., Vogel, B., Tao, M., Hoppe, C. M., Günther, G., Spelten, N., Hoffmann, L., Pumphrey, H.-C., Viciani, S., D’Amato, F., Volk, C. M., Hoor, P., Schlager, H., and Riese, M.: Tropical troposphere to stratosphere transport of carbon monoxide and long-lived trace species in the Chemical Lagrangian Model of the Stratosphere (CLaMS), *Geosci. Model Dev.*, 7, 2895–2916, <https://doi.org/10.5194/gmd-7-2895-2014>, 2014.
- Redington, A., Derwent, R., Witham, C., and Manning, A.: Sensitivity of modelled sulphate and nitrate aerosol to cloud, pH and ammonia emissions, *Atmos. Environ.*, 43, 3227–3234, <https://doi.org/10.1016/j.atmosenv.2009.03.041>, 2009.
- Rieger, V. S., Mertens, M., and Grewe, V.: An advanced method of contributing emissions to short-lived chemical species (OH and HO<sub>2</sub>): the TAGGING 1.1 submodel based on the Modular Earth Submodel System (MESSy 2.53), *Geosci. Model Dev.*, 11, 2049–2066, <https://doi.org/10.5194/gmd-11-2049-2018>, 2018.
- Rolph, G., Draxler, R., and Depena, R.: Modeling Sulfur Concentrations and Depositions in the United-States During Anatex, *Atmos. Environ.*, 26, 73–93, [https://doi.org/10.1016/0960-1686\(92\)90262-J](https://doi.org/10.1016/0960-1686(92)90262-J), 1992.
- Rößler, T., Stein, O., Heng, Y., Baumeister, P., and Hoffmann, L.: Trajectory errors of different numerical integration schemes diagnosed with the MPTRAC advection module driven by ECMWF operational analyses, *Geosci. Model Dev.*, 11, 575–592, <https://doi.org/10.5194/gmd-11-575-2018>, 2018.
- Sander, R., Baumgaertner, A., Cabrera-Perez, D., Frank, F., Gromov, S., Grooß, J.-U., Harder, H., Huijnen, V., Jöckel, P., Karydis, V. A., Niemeyer, K. E., Pozzer, A., Riede, H., Schultz, M. G., Taraborrelli, D., and Tauer, S.: The community atmospheric chemistry box model CAABA/MECCA-4.0, *Geosci. Model Dev.*, 12, 1365–1385, <https://doi.org/10.5194/gmd-12-1365-2019>, 2019.

- Sandu, A. and Sander, R.: Technical note: Simulating chemical systems in Fortran90 and Matlab with the Kinetic PreProcessor KPP-2.1, *Atmos. Chem. Phys.*, 6, 187–195, <https://doi.org/10.5194/acp-6-187-2006>, 2006.
- Seinfeld, J. H. and Pandis, S. N.: *Atmospheric chemistry and physics: from air pollution to climate change*, 3rd edn., John Wiley & Sons, ISBN 978-1-119-22117-3, 2016.
- Stavrakou, T., Müller, J.-F., Boersma, K. F., van der A, R. J., Kurokawa, J., Ohara, T., and Zhang, Q.: Key chemical NO<sub>x</sub> sink uncertainties and how they influence top-down emissions of nitrogen oxides, *Atmos. Chem. Phys.*, 13, 9057–9082, <https://doi.org/10.5194/acp-13-9057-2013>, 2013.
- Stein, A. F., Lamb, D., and Draxler, R. R.: Incorporation of detailed chemistry into a three-dimensional Lagrangian–Eulerian hybrid model: application to regional tropospheric ozone, *Atmos. Environ.*, 34, 4361–4372, [https://doi.org/10.1016/S1352-2310\(00\)00204-1](https://doi.org/10.1016/S1352-2310(00)00204-1), 2000.
- Stevenson, D. S., Collins, W. J., Johnson, C. E., and Derwent, R. G.: Intercomparison and evaluation of atmospheric transport in a Lagrangian model (STOCHEM), and an Eulerian model (UM), using 222Rn as a short-lived tracer, *Q. J. Roy. Meteor. Soc.*, 124, 2477–2491, <https://doi.org/10.1002/qj.49712455115>, 1998.
- Stohl, A., Forster, C., Frank, A., Seibert, P., and Wotawa, G.: Technical note: The Lagrangian particle dispersion model FLEXPART version 6.2, *Atmos. Chem. Phys.*, 5, 2461–2474, <https://doi.org/10.5194/acp-5-2461-2005>, 2005.
- Stohl, A., Seibert, P., Wotawa, G., Arnold, D., Burkhardt, J. F., Eckhardt, S., Tapia, C., Vargas, A., and Yasunari, T. J.: Xenon-133 and caesium-137 releases into the atmosphere from the Fukushima Dai-ichi nuclear power plant: determination of the source term, atmospheric dispersion, and deposition, *Atmos. Chem. Phys.*, 12, 2313–2343, <https://doi.org/10.5194/acp-12-2313-2012>, 2012.
- Tan, Z., Lu, K., Hofzumahaus, A., Fuchs, H., Bohn, B., Holland, F., Liu, Y., Rohrer, F., Shao, M., Sun, K., Wu, Y., Zeng, L., Zhang, Y., Zou, Q., Kiendler-Scharr, A., Wahner, A., and Zhang, Y.: Experimental budgets of OH, HO<sub>2</sub>, and RO<sub>2</sub> radicals and implications for ozone formation in the Pearl River Delta in China 2014, *Atmos. Chem. Phys.*, 19, 7129–7150, <https://doi.org/10.5194/acp-19-7129-2019>, 2019.
- Theys, N., De Smedt, I., Yu, H., Danckaert, T., van Gent, J., Hörmann, C., Wagner, T., Hedelt, P., Bauer, H., Romahn, F., Pedergnana, M., Loyola, D., and Van Roozendaal, M.: Sulfur dioxide retrievals from TROPOMI onboard Sentinel-5 Precursor: algorithm theoretical basis, *Atmos. Meas. Tech.*, 10, 119–153, <https://doi.org/10.5194/amt-10-119-2017>, 2017.
- U.S. Committee on Extension to the Standard Atmosphere (COESA): U.S. Standard Atmosphere, 1976, National Oceanic and Atmospheric Administration, National Aeronautics and Space Administration, United States Air Force, Washington, D.C., USA, <https://ntrs.nasa.gov/citations/19770009539> last access: 25 March 2025, 1976.
- Veefkind, J., Aben, I., McMullan, K., Förster, H., de Vries, J., Otter, G., Claas, J., Eskes, H., de Haan, J., Kleipool, Q., van Weele, M., Hasekamp, O., Hoogeveen, R., Landgraf, J., Snel, R., Tol, P., Ingmann, P., Voors, R., Kruizinga, B., Vink, R., Visser, H., and Levelt, P.: TROPOMI on the ESA Sentinel-5 Precursor: A GMES mission for global observations of the atmospheric composition for climate, air quality and ozone layer applications, *Remote Sens. Environ.*, 120, 70–83, <https://doi.org/10.1016/j.rse.2011.09.027>, 2012.
- Webster, H. N. and Thomson, D. J.: Using Ensemble Meteorological Data Sets to Treat Meteorological Uncertainties in a Bayesian Volcanic Ash Inverse Modeling System: A Case Study, Grímsvötn 2011, *J. Geophys. Res.*, 127, e2022JD036469, <https://doi.org/10.1029/2022JD036469>, 2022.
- Wohlmann, I. and Rex, M.: The Lagrangian chemistry and transport model ATLAS: validation of advective transport and mixing, *Geosci. Model Dev.*, 2, 153–173, <https://doi.org/10.5194/gmd-2-153-2009>, 2009.
- Wu, X., Griessbach, S., and Hoffmann, L.: Equatorward dispersion of a high-latitude volcanic plume and its relation to the Asian summer monsoon: a case study of the Sarychev eruption in 2009, *Atmos. Chem. Phys.*, 17, 13439–13455, <https://doi.org/10.5194/acp-17-13439-2017>, 2017.
- Wu, X., Griessbach, S., and Hoffmann, L.: Long-range transport of volcanic aerosol from the 2010 Merapi tropical eruption to Antarctica, *Atmos. Chem. Phys.*, 18, 15859–15877, <https://doi.org/10.5194/acp-18-15859-2018>, 2018.